Fermi National Accelerator Laboratory

FERMILAB-FN-609
TESLA NOTE 93-38

Positron Target Geometries for TESLA

A. Van Ginneken

Fermi National Accelerator Laboratory
P.O. Box 500, Batavia, Illinois 60510

September 1993

Operated by Universities Research Association Inc. under Contract No. DE-AC02-76CHO3000 with the United States Department of Energy

Disclaimer

This report was prepared as an account of work sponsored by an agency of the United States Government. Neither the United States Government nor any agency thereof, nor any of their employees, makes any warranty, express or implied, or assumes any legal liability or responsibility for the accuracy, completeness, or usefulness of any information, apparatus, product, or process disclosed, or represents that its use would not infringe privately owned rights. Reference herein to any specific commercial product, process, or service by trade name, trademark, manufacturer, or otherwise, does not necessarily constitute or imply its endorsement, recommendation, or favoring by the United States Government or any agency thereof. The views and opinions of authors expressed herein do not necessarily state or reflect those of the United States Government or any agency thereof.

Positron Target Geometries for TESLA

A. Van Ginneken
Fermi National Accelerator Laboratory*
P. O. Box 500, Batavia, IL 60510

August 1993

Abstract

Positron production in planar and tubular targets via wiggler radiated γs is investigated. Such targets offer distinct advantages over the canonical solid cylinders. Results of Monte Carlo simulations on a sampling of such targets are reported and compared with results for solid cylinders.

1 Introduction

This note concerns the production of positrons for use in TESLA or other proposed high energy e^+e^- colliders. More specifically it enlarges on a scheme of generating e^+ via photons radiated by the 'spent' e^- beam as it traverses a set of wiggler magnets [1]. Calculations exploring this method, as part of a preliminary e^+ source design for TESLA, have been reported for solid targets of various composition and moderate thickness [2]. The main theme here is consideration of different beam-target geometries and their effect on e^+ yield and energy depostion in the target. The geometries explored here consist of a wiggler followed by a target which is either a thin plate or pipe. Wiggler photons strike the planar surface of the plate, or *inner* surface of the pipe, at a shallow angle and induce an electromagnetic shower in the

*Work supported by the U.S. Department of Energy under contract No. DE-AC02-76CHO3000.

target. Some of the shower particles will escape via the same surface, i.e., are deflected back out. In pipe geometries, such particles may re-enter the target downstream—and continue the shower—or exit the pipe from its interior. For both target types, positrons are examined upon exiting the geometry as candidates for inclusion in the initial e^+ beam. Positron *collection* is not addressed in detail here. Instead, some simple cuts are imposed on the momentum of the produced positrons to estimate the amount collected. In addition to e^+ yield, energy deposition density (ρ_E) in the target is studied in some detail.

The geometry envisioned for plate targets is sketched in Fig. 1a. The e^- beam wiggles in the (vertical) YZ' plane. For a short stretch of wiggler, the 'spot' made by the γs on the target face is, to first order, determined vertically by the angular range of the wiggler oscillations times the wiggler-to-target distance, D_w. Horizontally (along Z) the spot is defined by the angles of the γs out of the wiggler plane times D_w and divided by the angle between wiggler axis and target surface. Vertically (along Y) the spot is thus very nearly uniform between rather sharp limits. The horizontal variation is a bit more complicated though it is well known and easily included in simulations. Roughly speaking, it is a superposition of Gaussians characterized by the photon energy (E_γ). Both amplitude and width of the Gaussians decline with E_γ. The latter implies—happily, for the present purpose—better focusing of the more energetic photons.

Pipe targets may be thought of as consisting of a combination of such plate targets. The e^- beam proceeds through a set of wigglers which 'point' to different spots on the inside pipe surface. Alternatively, helical type wigglers may provide more uniform irradiation. This note does not venture beyond these simplistic notions of wiggler/target geometries—which can be imagined to be quite complicated. The main purpose here is to investigate the merits of these targets *vs* solid cylinders in as simple a setting as possible. The outcome of this may then decide whether or not to pursue more realistic simulations. For pipe targets it is assumed here that the synchrotron radiation from the wiggler is distributed uniformly over the interior of the target pipe with fixed angle of incidence. This is an idealization and deviations from it will affect both energy deposition and e^+ yield although some of the lack of uniformity of the incident synchrotron radiation on the pipe wall gets washed out by the spread of the electromagnetic showers and by the phase space of the e^- beam if the latter were taken into account. Computationally, a great virtue of this arrangement—which the plate geometry lacks—is its cylindrical symmetry. The reduction to two dimensions makes

pipe simulations converge much quicker and greatly simplifies their analysis.

Throughout it is assumed that the e^- beam has an energy of 250 GeV and that the wiggler has a magnetic field of 1.8 Tesla. Even after fixing these, and with the simplifications already introduced, there remain a number of parameters to explore for the pipes: material, diameter, and length of the pipe as well as the incident angle of the synchrotron radiation. In addition, it appears advantageous to irradiate only the front part of the pipe so as to leave room for the positrons to emerge before encountering the collection device. This introduces yet another parameter: *target* length ($\leq$ *pipe* length). There are even more parameters for plate targets: material, target dimensions, angular range of synchrotron radiation, distance and angle between wiggler and target. Spatial and angular distributions of the emerging e^+ have rotational symmetry for the pipes but only up-down (Y) symmetry for plates leading to at least one more parameter for the latter: the angle between target and collection device (θ_c in fig. 1a). Again the preference—from an analysis standpoint—of pipe targets over plates is obvious from these parameter lists.

Below, sec. 2 briefly describes the model of the calculations. Sec. 3 presents some results on pipe and plate targets as well as a limited comparison with solid cylinders. Concluding remarks are in sec. 4.

2 Calculations

All calculations reported here are basically Monte Carlo simulations of photon induced electromagnetic showers. These are performed with the program EGS [3] which is a weighted simulation of $e-\gamma$ cascades in arbitrary 3-D geometry. For the present purpose three key ingredients must be added to the standard version: (1) selection of the incident γ energy and angle from the distributions appropriate for synchrotron radiation [4], (2) propagation of showers in the presence of an edge, and (3) angular distributions of pair production and bremsstrahlung.

Simulation of synchrotron radiation is readily incorporated into the Monte Carlo. As in all of EGS, particle selection is biased proportional to energy and the photon thus incurs a weight proportional to $1/E_\gamma$ [5]. First the angle (colatitude) is selected in straightforward fashion from the energy-integrated, energy-weighted differential cross section. Then—given the chosen angle—the energy is selected using table lookup (this involves Bessel fuctions $K_{1/3}$ and $K_{2/3}$). For the pipe geometry, the emission angle does

not enter directly into the present simulations in view of the assumption of a fixed angle of incidence with respect to the pipe axis. Photons below 5 MeV are not traced through the geometry since they contribute little to e^+ production and necessitate only a small ($\sim 2\%$) correction to energy deposition results. Fig. 1b shows a photon energy spectrum radiated by 250 GeV e^- in a 1.8 T field as generated in a typical; Monte Carlo run.

The presence of an edge requires special care [6]. As in [6] Coulomb scattering of $e^{\pm}$ is divided into small and large angle scattering with the former treated in the Gaussian approximation and the latter as discrete events. Most of the rest of [6] deals specifically with straight edges [7]. To accommodate curved surfaces, as for the pipes, the algorithm employed here steps between discrete events as though the particle were in a homogeneous medium. Given initial coordinates and direction (x_0, x_0', y_0, y_0'), those at the end of the step (x_1, x_1', y_1, y_1') are determined by sampling the Fermi distribution of multiple scattering (separately for x and y). If the new location is inside the wall it must still be ascertained whether or not the particle's trajectory has crossed the boundary since the Fermi distribution sums over *all* trajectories in a homogeneous target. If so, location and direction of escape must be determined. Even with x_1, y_1 outside the pipe wall it is generally necessary to pinpoint (x, x', y, y') at escape more accurately than is possible from the information at the end points. Either way one proceeds by determining coordinates and direction at mid-step where the distribution is particularly simple: an uncorrelated biGaussian with parameters

$$\langle x \rangle = \frac{(x_1 + x_0)}{2} - \frac{(x_1' - x_0')z}{8} \tag{1}$$

$$\sigma_x = \frac{\theta_s z^{3/2}}{8\sqrt{6}} \tag{2}$$

$$\langle x' \rangle = \frac{3(x_1 - x_0)}{2z} - \frac{(x_1' + x_0')z}{4} \tag{3}$$

$$\sigma_{x'} = \frac{\theta_s \sqrt{z}}{4\sqrt{2}} \tag{4}$$

where θ_s is the rms scattering angle, redefined to exclude large angle scattering [6]. There is a similar distribution for y, y'. The above expressions form the basis of an iterative algorithm. The distance from the boundary is determined at mid-step from eqs. 1 and 2 (plus their y counterparts) and also by extrapolation from each (x_0, x_0', y_0, y_0') and (x_1, x_1', y_1, y_1'). These

three distances are then tested *vs* a criterion based on σ_z from eq. 2. If all three remain inside the wall (along with x_1, y_1) and if their product exceeds $100\sigma_z^3$ [8] it is assumed that the particle has remained inside the wall the entire step. If all three (and x_1, y_1) are outside the wall and their product likewise exceeds $100\sigma_z^3$ it is assumed the particle has crossed the boundary in that half–step. The direction at the crossing is then determined from the locations inside and ouside the wall. If neither condition is fulfilled, x' and y' at midsegment are determined and the iteration proceeds on the lower half of the last z-segment. Since $\sigma_z^3 \propto z^{9/2}$, each reduction in steplength by a factor of two eases the test requirements considerably.

In electromagnetic showers, the angular spread due to pair production (or bremsstrahlung) can ordinarily be neglected when compared to that incurred from multiple Coulomb scattering. But in the present problem—where a photon strikes a surface at a shallow angle—the very first deflection encountered is, typically, associated with pair production, and this may already direct a member of the pair back out of the wall. Therefore after selecting the energy of the outgoing particle in a pair production or bremsstrahlung event, its angle is chosen from the appropriate differential cross section [9] and included in the shower simulation.

Monte Carlo results of ρ_E as a function of location are in the form of 2-D (pipes) or 3-D (plates) histograms over a set of bins which cover the entire target. Energy deposition is also calculated within a set of thin layers near the inner surface. The small volumes associated with the thin layer ρ_Es cause considerable statistical uncertainty in a typical Monte Carlo run. Accordingly, these results are smoothed out [10] and ρ_E^{max} is then estimated assuming ρ_E peaks at the surface. Smoothing is also applied to the e^+ momentum spectra. Calculations for solid targets use essentially the same code minus the worries about edge escape.

3 Results

The main outputs of the calculations are energy deposition density, ρ_E, as a function of location within the target and a set of distributions of the produced e^+ as well as of e^- and γ. For a first look at an entire array of targets of diverse composition and geometry it is convenient to condense these outputs to a few numbers for each case. With respect to ρ_E two results merit particular attention: the integral of ρ_E over the entire target (E_{tot}) and its maximum value within the target (ρ_E^{max}) [11], obtained as

stated above. The latter is concerned with target integrity over short time scales and the former with possible cooling requirements to avoid longer term heating problems. Positron yield information is likewise condensed into two numbers: total e^+ at the end of the target and those suitable for capture in an initial e^+ beam. For simplicity this is assumed to comprise all e^+ inside an area of about one cm^2 (the precise delineation of which depends on target type), an exit angle within 50 mrad, and p_z within 25% of some central p_z^0 chosen so as to optimize the yield. These are referred to here as 'accepted' e^+. In the manner of [2] all results below are normalized to one beam electron passing through one meter of wiggler.

3.1 Plate Targets

As mentioned in the Introduction and illustrated in fig. 1a, the plate geometry consists of a target, assumed to lie in the (vertical) YZ plane and a wiggler with axis along Z' and orbits in the (vertical) YZ' plane. The Z and Z' axes cross at the origin, making a small angle θ_w. Neglecting beam size and angular dispersion, the photons strike the target at $z = D_w\theta_\gamma/\theta_w$ where θ_γ is the angle between e^- and γ out of the wiggler plane (colatitude). The y distribution at impact is nearly uniform between $y = \pm D_w\theta_e^{max}$ where θ_e^{max} is the largest angle between the electron orbit and the wiggler axis. Given the field (1.8 T) and energy (250 GeV) of the e^-, specifying θ_e^{max} fixes the wiggler wavelength—typically of order 10 cm here. Fig. 1c shows total photon energy incident on a plate target as a function of location as generated in a typical Monte Carlo run with $\theta_e^{max} = \theta_w$ =0.1 mrad, $t_{1/2}$ =50 cm, and $D_w = 30\ m$.

In this somewhat simplified picture all γs have $x' = \theta_w + \theta_\gamma \simeq \theta_w$ and $y' = \theta_e$ is uniquely correlated with $y = D_w\theta_e$ at impact. Excluding a small fraction emanating from the back of the target, the e^+ emerge with $x' < 0$. It pays therefore to align the collection device at some angle θ_c with respect to the target. Here θ_c is held constant at -25 mrad which is close to the average angle of the accepted e^+ for all cases analyzed. For all results reported here the target extends out to $-\infty$ along Z, unlike in fig. 1a where a shorter target is shown for clarity, though obviously few accepted e^+ originate at large negative z. An accepted e^+ is required to have exit coordinates $x \geq -1$ cm, $|y| \leq 0.65$ cm, and to be within the above mentioned constraints on p_z and θ (measured with respect to θ_c).

Table I compares yields and energy densities for a limited number of plate target geometries. Target materials (here and below) are beryllium,

aluminum, iron, and tungsten. Target size is varied relatively little with thickness held constant at 1 mm, while the lateral area is chosen to accommodate the 'spot' size of the γs striking it. The latter may be defined as $\Delta Y \times \Delta Z$ where $\Delta Y = D_w \theta_e^{max}$ and $\Delta Z = D_w \langle \theta_\gamma \rangle / \theta_w$. For this purpose $\langle \theta_\gamma \rangle \approx 1/\gamma \equiv m_e/E_{e^-}$ ($\approx 2\,\mu$rad for 250 GeV e^-). Target (half) height (ΔY) is kept constant at 0.6 cm while (half) width (ΔZ) is varied over a limited range. The angles θ_e^{max} and θ_w, which are at one's disposal, are likewise kept within narrow limits. Table I lists total and total accepted e^+ which depend only moderately on target and geometry. Also in the table are total energy deposited in the (1 mm thick) target and ρ_E^{max}. Not surprisingly both are substantially larger in the heavier targets. Table I also lists the ratio: $(accepted\ e^+)/\rho_E^{max}$. For targets of the same composition but different type or dimensions this number may be said to measure relative target efficiency. Comparison among targets of different composition should include their thermal and mechanical properties. The variation of target efficiency—so defined—seems to indicate that an optimum exists within the parameter set of table I, though serious attempts at optimization should await more complete simulations and analysis.

For an aluminum target with both θ_e^{max} and θ_w at 0.1 mrad, target half length ($t_{1/2}$) of 50 cm, and D_w of 30 meters, fig. 2 shows scatter plots of the x, y distribution at the end of the target of γs, e^-s, and of total and accepted e^+s. All four have the same normalization which fixes the maximum of e^+ per bin at 40. This convention is followed in all similar figures below. It permits, within the limited range of these plots, to clearly display the location of maximum density of produced e^+ as well as the density variation in its vicinity. It can be seen that, due to Compton scattering, e^- are somewhat more numerous (by about 20%) than e^+ [12]. Staying with the same target/wiggler geometry, fig. 3 presents x, x' and y, y' distributions of both total and accepted e^+. Both figs. 2 and 3 demonstrate—as stated earlier—that relatively little is contributed by e^+ emerging from the back of the target (i.e., with $x > 0$). Fig. 4 shows, for all e^+, the momentum (p) and perpendicular momentum ($p_\perp$) spectra as well as their (smoothed) correlation. A diagonal across fig. 4c corresponds to the angular 50 mrad cut with those above it rejected. For beryllium and tungsten targets—with the same geometry as above—fig. 5 displays, as a function of z, the number of γs which lead to an accepted e^+. On the same graph is shown the distribution of the z-coordinate at which accepted e^+s exit the plate's surface. These two distributions are expected to be displaced by a distance of the order of a radiation length (X_0). On the scale of fig. 5 this makes

them virtually coincident for tungsten (X_0=0.35 cm) but well separated in the case of beryllium (X_0=35.3 cm).

3.2 Pipe Targets

To restate briefly the model for pipe targets: photons with energy spectrum generated by 250 GeV e^- traversing a 1.8 T wiggler are directed to the inner surface of a pipe of given diameter and wall thickness. The photons are assumed to be uniformly distributed over the pipe's inner surface. The photon direction is at some fixed angle with respect to the pipe axis and its trajectory is assumed to originate on the axis (i.e., $\phi' = 0$ where ϕ is the azimuthal angle). A limited set of incident angles is explored. Here accepted e^+ have $r \leq 0.6$ cm along with the above constraints on θ and p_z.

As mentioned such an incident photon flux may be furnished by a helical wiggler with pitch angle equal to the incident photon angle [13]. For 0.1 mrad incident γs from 250 GeV e^-s, a 1 m pipe contains the radiation much like 1 m plate in the 0.1 mrad, D_w=50 m case. More uniform illumination may be provided if, e.g., pitch angle is made to vary with distance along the wiggler. Again, the e^- beam emittance will tend to blur the correlation between photon energy and point of incidence.

For most cases analyzed here target length is taken equal to pipe length but shorter targets are briefly examined. Table II presents results for a sample of pipe targets of the adopted standard materials and with indicated angle of incident γs and pipe radius. All have length of 100 cm. While a few results for an inner radius of 0.3 cm are shown, most have r=0.5 cm which has favored status since—with the 0.1 cm thick pipe wall added—it coincides with the assumed radial upper limit for collection. The gain in accepted yield with increasing target mass appears to be more than offset by increases in ρ_E^{max} and E_{tot}. Decreasing the angle of incidence also benefits accepted yields but with large growth in ρ_E^{max} while E_{tot} declines moderately.

Scaling arguments may be used to estimate yields for pipes with dimensions simply related to those specified in a Monte Carlo run. Most accepted e^+ are created by showers at shallow depths in the pipe wall, i.e., radial penetration is much smaller than pipe radius. To a lesser extent this remains true in the longitudinal direction (see, e.g., fig. 5 which compares longitudinal penetration in beryllium and tungsten). If penetration were entirely negligible a simple rule would result: by scaling the problem equally in all dimensions, the coordinates of particles crossing the exit plane of the pipe likewise scale by the same factor and the total number exiting the pipe via

its interior remains unchanged. Scaling thus implies that a pipe with radius equal to the collection limit is close to the optimum. For the same number of incident γs smaller pipes produce a higher e^+ density but do not add any more particles (while ρ_E^{max} increases). For larger pipes some e^+ cross the exit plane outside $r = 0.6$ cm and are thus 'lost' while particle densities in the central region are diluted. This scaling has been verified by Monte Carlo. For obvious reasons it works very well for tungsten yet remains reasonably good even for beryllium. Also for obvious reasons it cannot be applied where penetration distances are comparable to or exceed target dimensions, i.e., for targets shorter than a few radiation lengths. Note that such scaling does not extend to energy deposition which depends strongly on penetration distance.

Fig. 6 shows the effect of pipe length on accepted e^+ yield, on ρ_E^{max}, and on their ratio. Roughly, the latter appears to reach a plateau around 100 cm—independent of target species. For beryllium this also corresponds closely to the maximum in accepted yield. For a first look such one-meter-targets thus appear to be a reasonable choice. This is also the length adopted in most plate target simulations which makes pipes *vs* plates comparisons somewhat more significant. Results of a brief study of the aforementioned effect of making target length shorter than pipe length are shown in fig. 7 for a 100 cm long pipe of beryllium—which is the material where it should the most noticeable. Both accepted yield and maximum energy deposition are presented as ratios to 'target=pipe' results. Yields remain close to unity throughout while ρ_E^{max} closely matches the slight gain ($<\sim 10\%$) in accepted e^+ observed when target length decreases to ~ 70 cm. For much shorter targets ρ_E^{max} increases more rapidly with decreasing target length. These results illustrate—in a limited way and confined to the longitudinal direction—to what extent the showers wash out non-uniformity of the incident γs.

Figs. 8-10 show results for tubular targets similar to those presented for planar ones. All are for 100 cm long pipes and incident angle of 0.1 mrad. For an aluminum target, fig. 8 compares x, y plots of gross yields of γ, e^-, and e^+ along with that of accepted e^+. The latter is close to uniform over the interior exit face which may be of use in scaling applications. Fig. 9 presents combined x, x' and y, y' phase space plots of both total and accepted e^+ for beryllium and tungsten targets. Fig. 10 shows p and $p_\perp$ spectra of all e^+ for aluminum along with their correlation. Fig. 11 displays distributions of the maximum radial shower excursion, R_s^{max}, of accepted positrons in beryllium and tungsten pipes. R_s^{max} is the largest radial excursion of the shower—as measured from the inner pipe radius—preceding an accepted e^+. Thus, for

a pipe thinner than R_s^{max} the shower exits the exterior pipe wall and the e^+ in question fails to be created. Fig. 11 shows that all significant e^+ production occurs within a few microns of the inner surface which results from the small angles of the particles involved in creating an acceptable positron. Small radial distances thus correspond to long pathlengths and most e^+ created beyond a skin depth of a few microns are re-absorbed. Fig. 11 illustrates that radial scaling also works better for tungsten than for beryllium but the micron scale indicates that it should work well for all targets. Fig. 12 plots the radial dependence of the longitudinally integrated energy deposition density for beryllium and tungsten targets from which E_{tot} can be estimated as a function of pipe thickness.

3.3 Solid Cylinders

Table III contains some results for solid targets included here for comparison. Target lengths correspond to rounded values of 0.2, 0.4, and 0.6 radiation lengths with most attention paid to $0.4X_0$ [2]. It is assumed that the photon beam is uniform, of circular shape, without angular divergence. It is otherwise generated in the same way as for plates and pipes.

Fig. 13 shows x, y distributions of all e^+ and of accepted e^+ for a $0.4X_0$ long beryllium and tungsten targets with a beam radius of 0.3 cm. For the same targets, fig. 14 shows the combined x, x' and y, y' distributions–again of all e^+ and of accepted e^+. Much of figs. 13 and 14 is explained by noting that the beryllium target is exactly 100 times the length of the tungsten target. Fig. 15 shows the p and $p_\perp$ spectra for an aluminum target (3.6 cm long, 0.3 cm radius) which compares with figs. 4 and 10 for plates and pipes respectively. The spectra of fig. 15 peak at lower p and higher $p_\perp$ than those for plates or pipes which by virtue of their length and geometry tend to eliminate low-p, high-$p_\perp$ e^+s.

4 Concluding Remarks

In comparing the three target types much depends on which column in tables I–III is chosen, which in turn depends on what may prove to be the limiting factors in a realistic design. Target efficiency (last column) is broadly comparable though with a decided edge for the pipes. Total e^+ accepted is much higher for pipes and plates than for solids which implies a shorter wiggler can do the job. As listed, total energy deposited favors solid targets over pipe and plate targets. However, as already pointed out [11], there

is considerable arbitrariness in the choice of target thickness for plates and pipes which impacts E_{tot}. Since E_{tot} relates mostly to possible cooling requirements, it should be noted that pipes and plates are easier to cool by virtue of their geometry and their length. Planar and tubular targets appear also much simpler to integrate into the 250 GeV beamline as well as into the e^+ collection device. For example, a solenoidal field present in the interior of a pipe or plate target which increases in strength with z could provide focusing for the emerging e^+ beam and thus boost yields. With or without such a field a more detailed matching of collection device to target should be included in further studies. The strong dependence of momentum spectrum on wiggler/target geometry indicates that the generic cuts applied here are not of much value beyond taking a first look. It is clear also that further work is needed on optimization of target—type, size, and shape—and wiggler. It is likely that the latter will not just be an off-the-shelf type but will require some unique specifications. These and other variations on the present theme may be worth examining in the framework of a more realistic design study.

If a copious supply of e^+ is easily produced in this manner one might consider including its mirror process: e^- from the spent e^+ beam. A low energy e^- source is still needed to initiate the entire process, though with less demands placed on it. Following such initialization, beam intensities increase exponentially with time after which the production rate increase can be slowed toward achieving steady state at the desired intensities. This can be accomplished in a variety of ways by adjustments to wiggler, target, or collection device.

Acknowledgement. My thanks to H. Edwards for suggesting to include the plate targets and for many useful comments on the manuscript. Thanks also to D. Finley for his comments.

References

[1] V. E. Balakin and A. A. Mikhailichenko, Novosibirsk Preprint INP-79-85 (1979).

[2] K. Floettmann and J. Rossbach, DESY Preprint M-91-11 (1991); K. Floettmann, ECFA Workshop on e^+e^- Linear Colliders, Garmisch-Partenkirchen (1992).

[3] A. Van Ginneken, Fermilab Report FN-309 (1978).

[4] J. D. Jackson, *Classical Electrodynamics*, Wiley, New York (1967).

[5] In AEGIS the entire $e-\gamma$ shower is represented by a single, weighted e^+, e^-, or γ. Its selection is proportional to its energy which, in turn, is roughly proportional to its ability to propagate the shower and deposit energy in the target. This bias also serves well the present purpose, viz., creation of positrons.

[6] A. Van Ginneken, Phys. Rev. D37, 3292 (1988).

[7] Approximating the cylindrical edge with its (local) tangent plane does not work very well since e^+ energies are typically only of the order of tens of MeV leading to fairly large scattering angles and necessitating an iterative approach to locate the boundary crossing.

[8] This somewhat arbitrary measure makes an intermediate outside excursion highly unlikely. These procedures could be refined but results appear rather insensitive to the precise scheme employed.

[9] Y.-S. Tsai, Rev. Mod. Phys. 46, 815 (1974).

[10] A. Van Ginneken, Nucl. Inst. Meth. A305, 453 (1991).

[11] For plates and pipes the utility of E_{tot} is diminished by its dependence on target thickness. Beyond a micron-sized skin any extra thickness contributes relatively more to E_{tot} than to e^+ yield. In a realistic design, target thickness is thus likely to be determined from considerations of mechanical strength and cooling efficiency—questions which are not addressed here. To make E_{tot} more meaningful, target thickness is kept constant (at 1 mm) throughout for plates and pipes. Interpretation of ρ_E^{max} is also somewhat ambiguous. Calculations show ρ_E to peak at (or extremely close to) the surface and then decline rapidly over a microscopic scale with distance into the target, e.g., for an aluminum pipe and incident angle of 0.1 mrad, ρ_E falls to ~70% of its maximum at a depth of 0.2 μ. It is not obvious that one can treat ρ_E in such a thin surface layer in the usual manner (i.e., as though it were inside of a typical thick target) with regard to heat transfer, melting, etc.

[12] The contribution from δ-rays to the e^+ yield—via bremsstrahlung followed by pair creation—is neglected here.

[13] B. M. Kincaid, J. Appl. Phys. 48, 2684 (1977). For the present purpose, the spread along the pipe in the z direction can be expressed as $\Delta = r_{pipe}/(\gamma\theta_p^2)$ where θ_p is the pitch angle of the wiggler and $\gamma = E/m$ for the beam e^-s.

TABLE I

PLANAR TARGETS

tgt mat	max e- angle mrad	wg/tgt angle mrad	tgt half length cm	wg/tgt distnce meter	total e+	total accptd	central mom MeV/c	fractn accptd	max E-dep GeV/cu.cm	total E-dep GeV	e+ acptd / max E-dep
Be	0.05	0.05	50	30	0.236	0.0451	63.6	0.19	0.098	0.0117	0.46
Be	0.05	0.1	50	30	0.318	0.0597	57.6	0.19	0.099	0.0133	0.61
Be	0.1	0.05	50	30	0.231	0.0448	62.4	0.19	0.051	0.0117	0.88
Be	0.1	0.1	25	30	0.255	0.0479	51.6	0.19	0.059	0.0089	0.83
Be	0.1	0.1	50	10	0.431	0.0794	49.2	0.18	0.351	0.0148	0.23
Be	0.1	0.1	50	30	0.313	0.0568	58.8	0.18	0.057	0.0133	1.03
Be	0.1	0.1	50	50	0.225	0.0416	63.6	0.18	0.023	0.0127	1.85
Be	0.1	0.1	75	30	0.310	0.0551	63.6	0.18	0.055	0.0173	1.00
Be	0.2	0.1	50	20	0.363	0.0673	54.0	0.19	0.059	0.0137	1.15
Be	0.1	0.2	50	30	0.360	0.0635	55.2	0.18	0.058	0.0157	1.09
Be	0.2	0.2	50	20	0.375	0.0581	52.8	0.17	0.058	0.0162	1.13
Al	0.05	0.05	50	20	0.431	0.0760	63.6	0.18	0.446	0.0172	0.17
Al	0.05	0.05	50	50	0.210	0.0355	70.8	0.17	0.091	0.0145	0.39
Al	0.1	0.1	50	30	0.447	0.0739	62.4	0.17	0.118	0.0200	0.63
Al	0.1	0.1	50	50	0.306	0.0504	68.4	0.16	0.048	0.0176	1.06
Al	0.2	0.2	50	20	0.480	0.0684	64.8	0.14	0.155	0.0269	0.44
Al	0.2	0.2	50	50	0.238	0.0356	62.4	0.15	0.026	0.0133	1.36
Fe	0.05	0.05	50	30	0.340	0.0560	68.4	0.16	0.711	0.0240	0.079
Fe	0.1	0.1	50	30	0.453	0.0693	62.4	0.15	0.390	0.0313	0.18
Fe	0.1	0.1	50	50	0.323	0.0499	67.2	0.15	0.142	0.0270	0.35
Fe	0.2	0.2	50	20	0.409	0.0476	73.2	0.13	0.503	0.0409	0.095
W	0.05	0.05	50	30	0.357	0.0567	67.2	0.16	1.582	0.0317	0.036
W	0.1	0.1	50	30	0.475	0.0679	61.2	0.14	0.870	0.0412	0.078
W	0.1	0.1	50	50	0.340	0.0501	61.2	0.15	0.460	0.0358	0.11
W	0.2	0.2	50	20	0.368	0.0453	74.4	0.12	1.154	0.0527	0.039
W	0.2	0.2	50	50	0.241	0.0305	61.2	0.13	0.192	0.0275	0.16

TABLE II

PIPE TARGETS

(PIPE LENGTH = TARGET LENGTH = 100 cm)

tgt mat	pipe radius cm	inc angle mrad	total e+	total accptd	central mom MeV/c	fractn accptd	max E-dep GeV/cu.cm	total E-dep GeV	tot acptd / max E-dep
Be	0.5	0.01	0.447	0.083	44.4	0.19	0.0305	0.0177	2.7
Be	0.5	0.1	0.322	0.056	51.8	0.17	0.0094	0.0210	6.0
Be	0.5	1.	0.167	0.023	63.6	0.13	0.0028	0.0246	8.0
Al	0.3	0.01	0.534	0.097	49.2	0.18	0.1375	0.0307	0.70
Al	0.3	0.1	0.329	0.052	55.2	0.16	0.0374	0.0352	1.39
Al	0.3	1.	0.161	0.0180	66.0	0.11	0.0102	0.0392	1.76
Al	0.5	0.01	0.752	0.135	44.4	0.18	0.0948	0.0283	1.43
Al	0.5	0.1	0.487	0.077	52.8	0.16	0.0225	0.0337	3.4
Al	0.5	1.	0.241	0.027	63.6	0.11	0.0069	0.0392	4.0
Fe	0.5	0.01	0.863	0.151	43.2	0.17	0.356	0.0551	0.42
Fe	0.5	0.1	0.545	0.084	52.8	0.15	0.0776	0.0645	1.08
Fe	0.5	1.	0.268	0.028	63.6	0.11	0.0226	0.0737	1.26
W	0.5	0.01	0.946	0.160	43.2	0.17	1.030	0.0754	0.15
W	0.5	0.1	0.598	0.089	52.8	0.15	0.223	0.0886	0.40
W	0.5	1.	0.297	0.031	63.6	0.10	0.0585	0.1013	0.52

TABLE III

SOLID CYLINDER TARGETS

tgt mat	tgt length cm	beam radius cm	total e+	total accptd	central mom MeV/c	fractn accptd	max E-dep GeV/cu.cm	total E-dep GeV	tot acptd / max E-dep
Be	7	0.3	0.147	0.0095	80.4	0.065	0.00460	0.0080	2.0
Be	14	0.1	0.156	0.0099	82.8	0.063	0.0212	0.0198	0.47
Be	14	0.3	0.152	0.0100	80.4	0.066	0.00437	0.0193	2.3
Be	14	0.5	0.139	0.0096	81.6	0.069	0.00214	0.0180	4.5
Be	21	0.3	0.137	0.0092	85.2	0.067	0.00428	0.0298	2.1
Al	1.8	0.3	0.265	0.0114	81.6	0.043	0.0109	0.0040	1.1
Al	3.6	0.1	0.356	0.0127	84.0	0.036	0.0702	0.0119	0.18
Al	3.6	0.3	0.349	0.0127	82.8	0.036	0.0135	0.0117	0.94
Al	3.6	0.5	0.328	0.0128	82.8	0.039	0.0060	0.0112	2.1
Al	5.4	0.3	0.359	0.0123	81.6	0.034	0.0134	0.0203	0.92
Fe	0.35	0.3	0.333	0.0122	76.8	0.037	0.0429	0.0023	0.28
Fe	0.70	0.1	0.515	0.0138	82.8	0.027	0.426	0.0082	0.032
Fe	0.70	0.3	0.513	0.0140	82.8	0.027	0.076	0.0082	0.18
Fe	0.70	0.5	0.504	0.0138	82.8	0.027	0.027	0.0080	0.51
Fe	1.05	0.3	0.610	0.0135	84.0	0.022	0.082	0.0160	0.16
W	0.07	0.3	0.415	0.0139	76.6	0.033	0.102	0.0012	0.14
W	0.14	0.1	0.703	0.0154	80.4	0.022	1.598	0.0045	0.0094
W	0.14	0.3	0.703	0.0154	80.4	0.022	0.200	0.0045	0.077
W	0.14	0.5	0.703	0.0154	81.6	0.022	0.064	0.045	0.24
W	0.21	0.3	0.881	0.0152	82.8	0.017	0.269	0.097	0.057

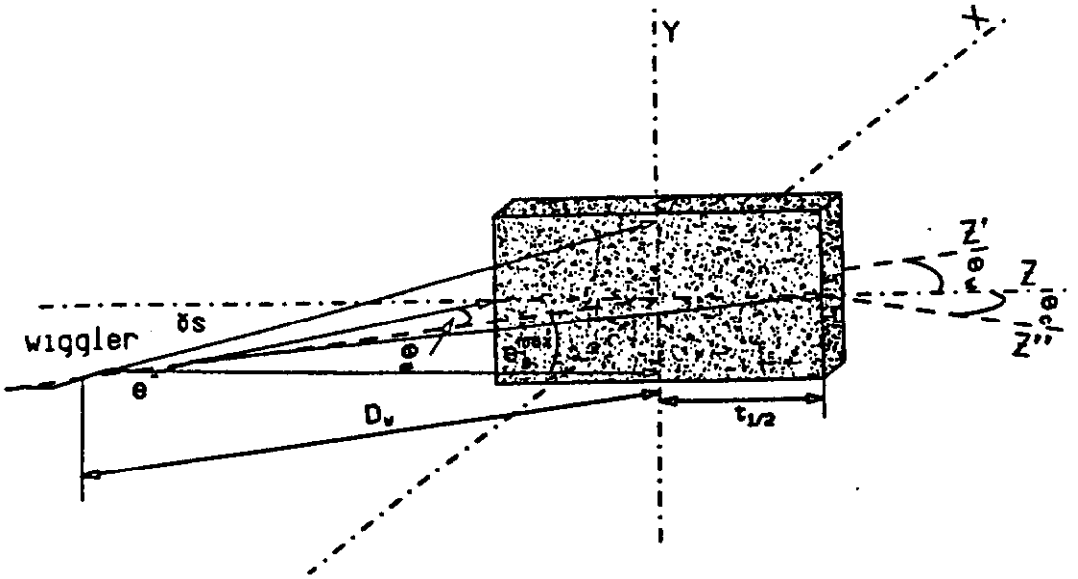

Fig. 1a Planar beam-target geometry with origin at center of target surface. Wiggler axis is along Z' in XZ plane, at angle θ_w to target surface. Electron beam oscillates in YZ' plane with maximum angle θ_e^{max} between e^- and wiggler axis. Collection device is along Z'' at angle θ_c in XZ plane. Length of wiggler is assumed small compared with distance to target, D_w.

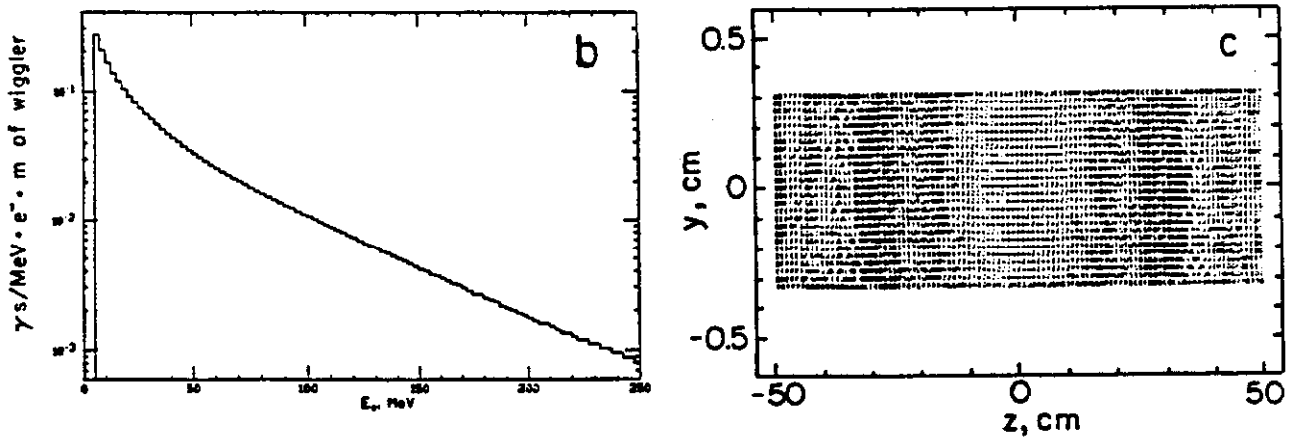

Fig. 1 (b) Spectrum of synchrotron radiation as generated in typical Monte Carlo run. Photons below 5 MeV are exluded from spectrum and from calculation. Photons above 250 MeV are included in calculation though not shown above. (c) Relative measure of total energy incident on plate target as a function of location for geometry: θ_w=0.1 mrad, θ_e^{max}=0.1 mrad, D_w = 30 m, and $t_{1/2}$=50 cm.

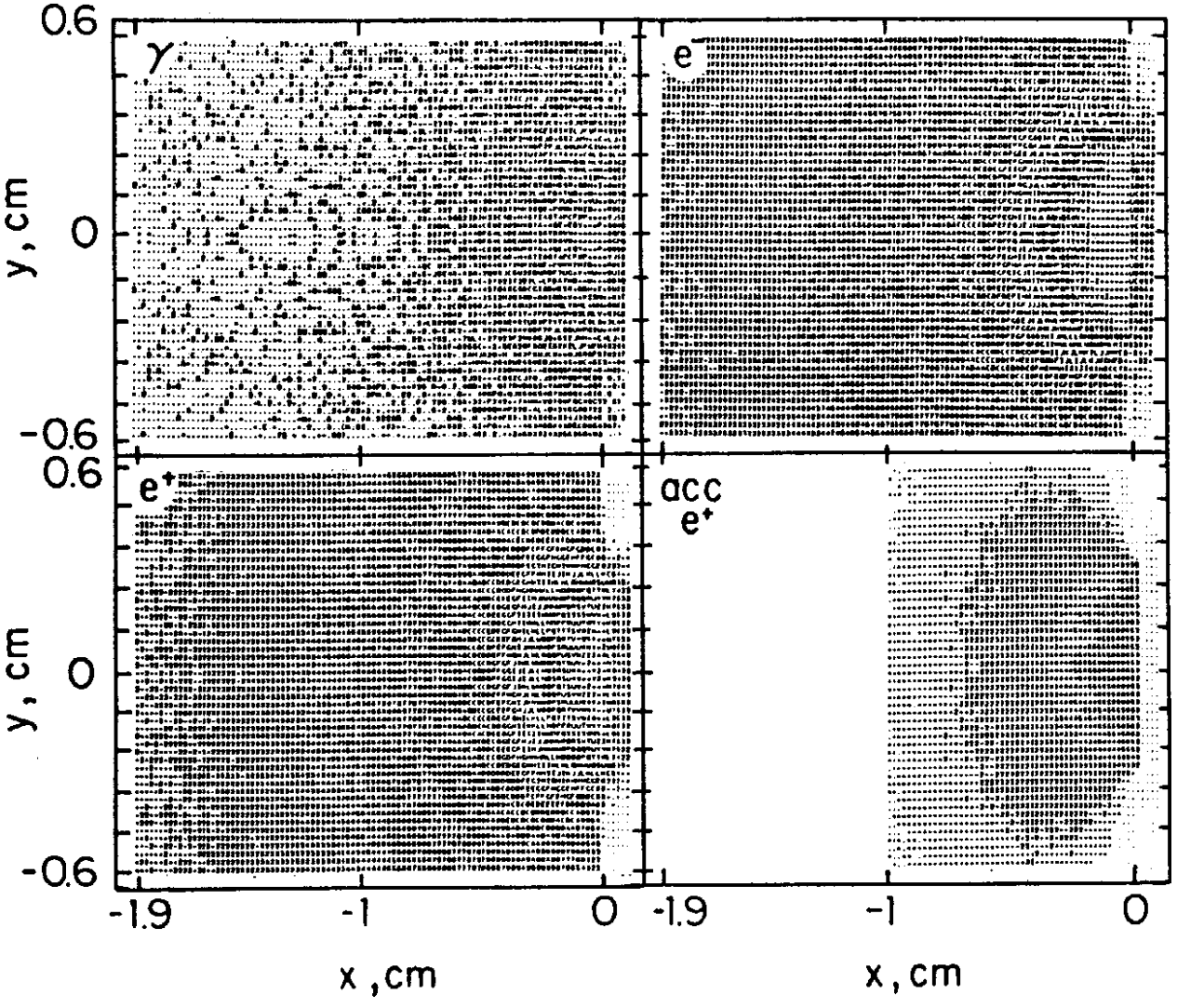

Fig. 2 Plots of z,y distribution for γs, e^-, e^+, and accepted e^+ at end of planar aluminum target with θ_w=0.1 mrad, θ_e^{max}=0.1 mrad, D_w = 30 m, and $t_{1/2}$=50 cm.

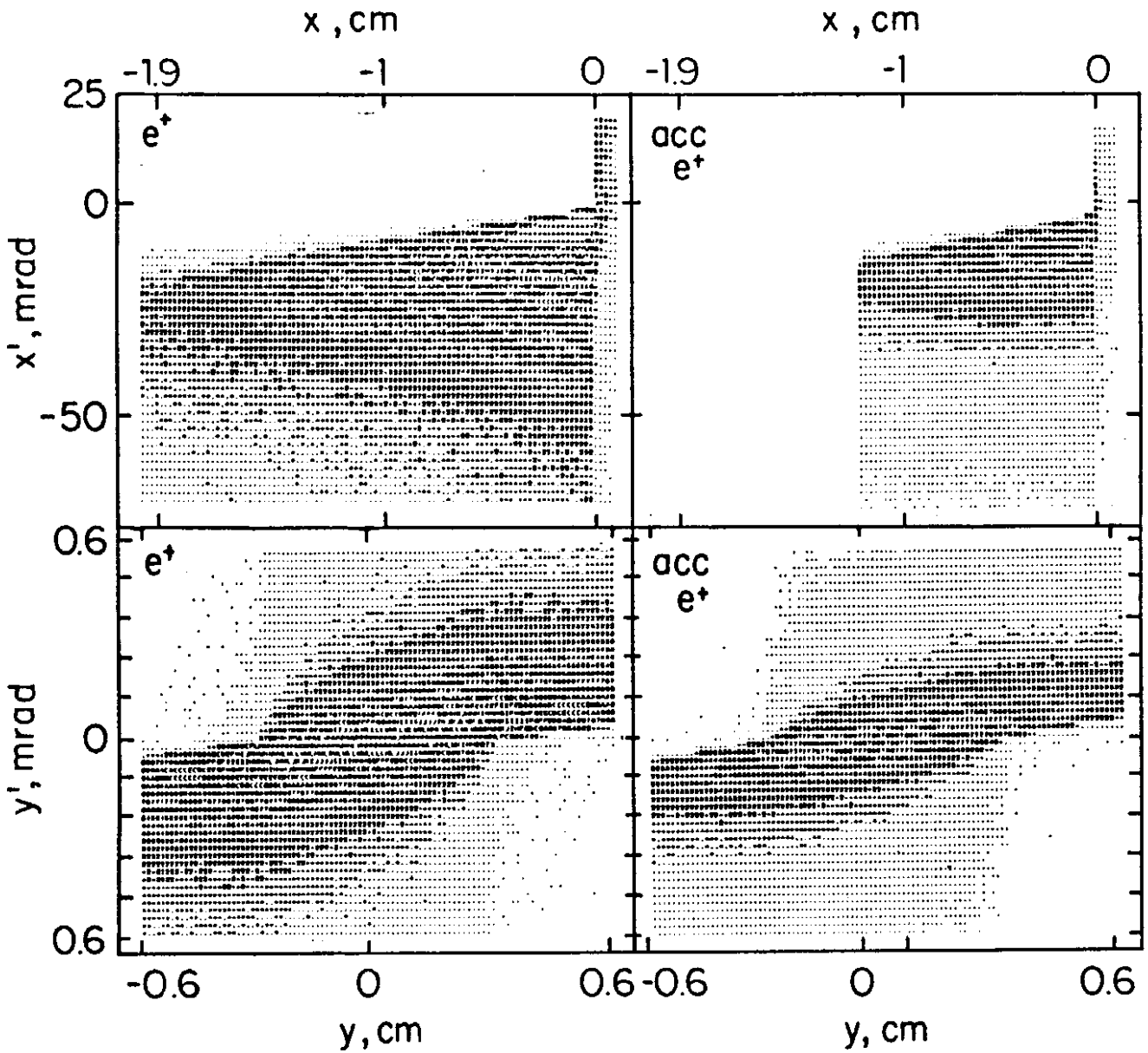

Fig. 3 Plots of x, x' (top) and y, y' distribution (bottom) for e^+ and accepted e^+ at end of planar aluminum target with θ_w=0.1 mrad, θ_e^{max}=0.1 mrad, D_w = 30 m, and $t_{1/2}$=50 cm.

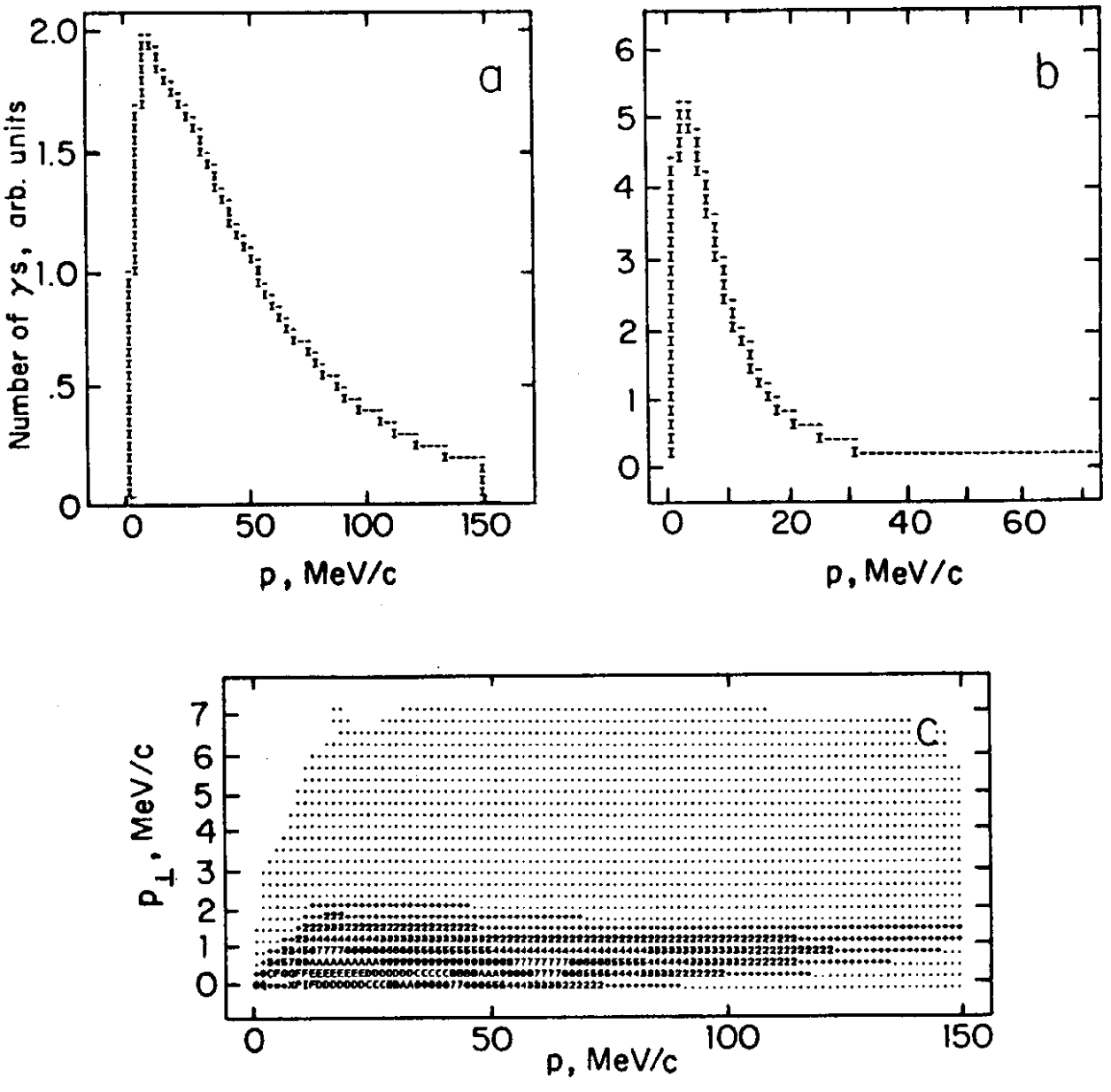

Fig. 4 (a) Momentum spectrum, (b) $p_\perp$ spectrum, and (c) joint distribution for all e^+ at end of planar aluminum target with θ_w=0.1 mrad, θ_e^{max}=0.1 mrad, D_w = 30 m, and $t_{1/2}$=50 cm.

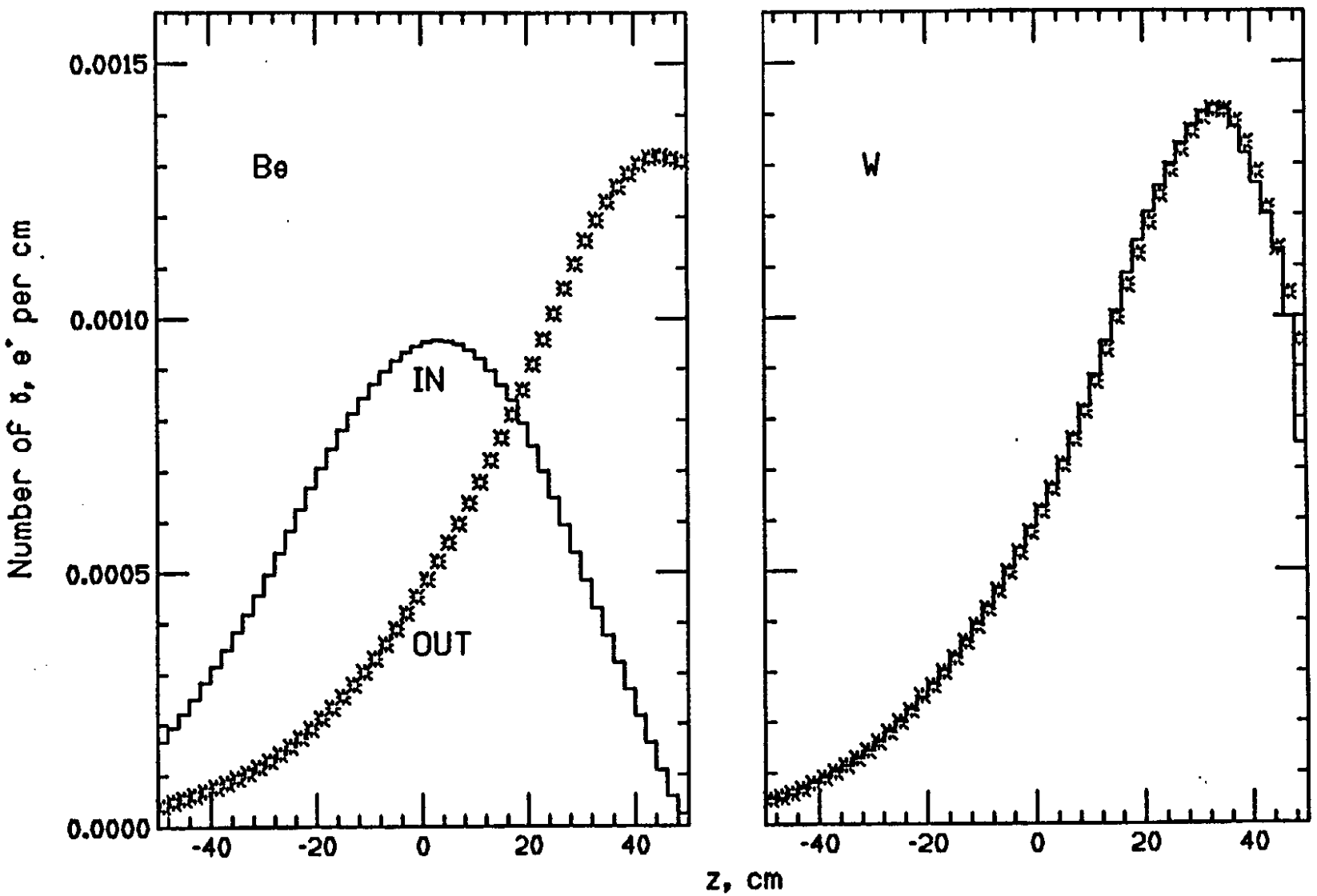

Fig. 5 Number of γs leading to accepted e^+ (histogram) and accepted e^+ exiting target (stars) per cm *vs* z for beryllium (left) and tungsten (right).

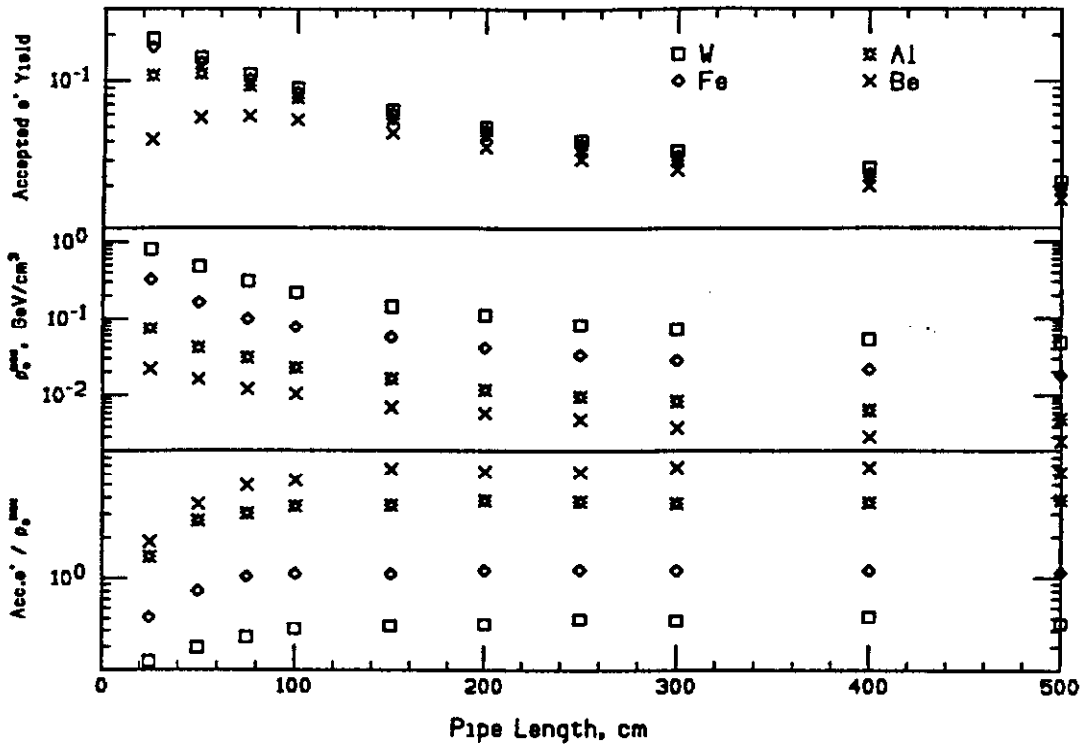

Fig. 6 Number of accepted e^+ (top) and maximum energy deposition in the target in GeV/cm^3 (middle) *vs* pipe length for four target species (per beam e^- and per meter of wiggler). Bottom graph is their ratio (e^+ per GeV/cm^3).

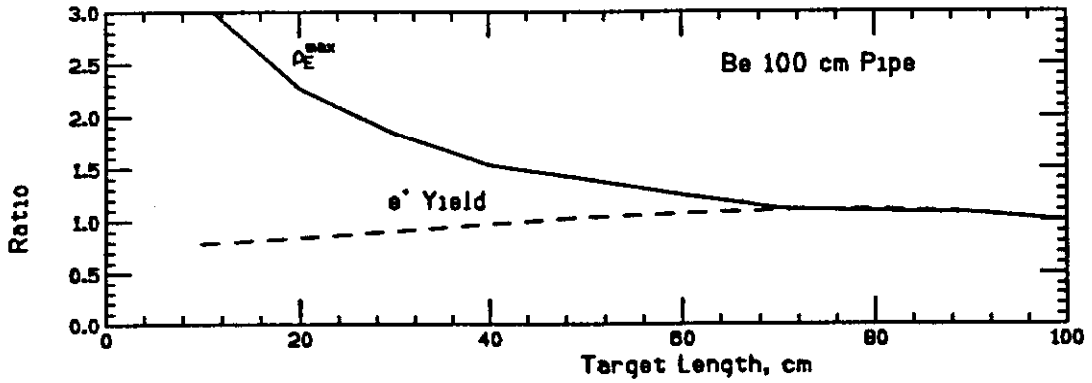

Fig. 7 Positron yield and ρ_E^{max} *vs* target length ($\leq$ pipe length) for 100 cm long beryllium pipe (relative to target length = pipe length values).

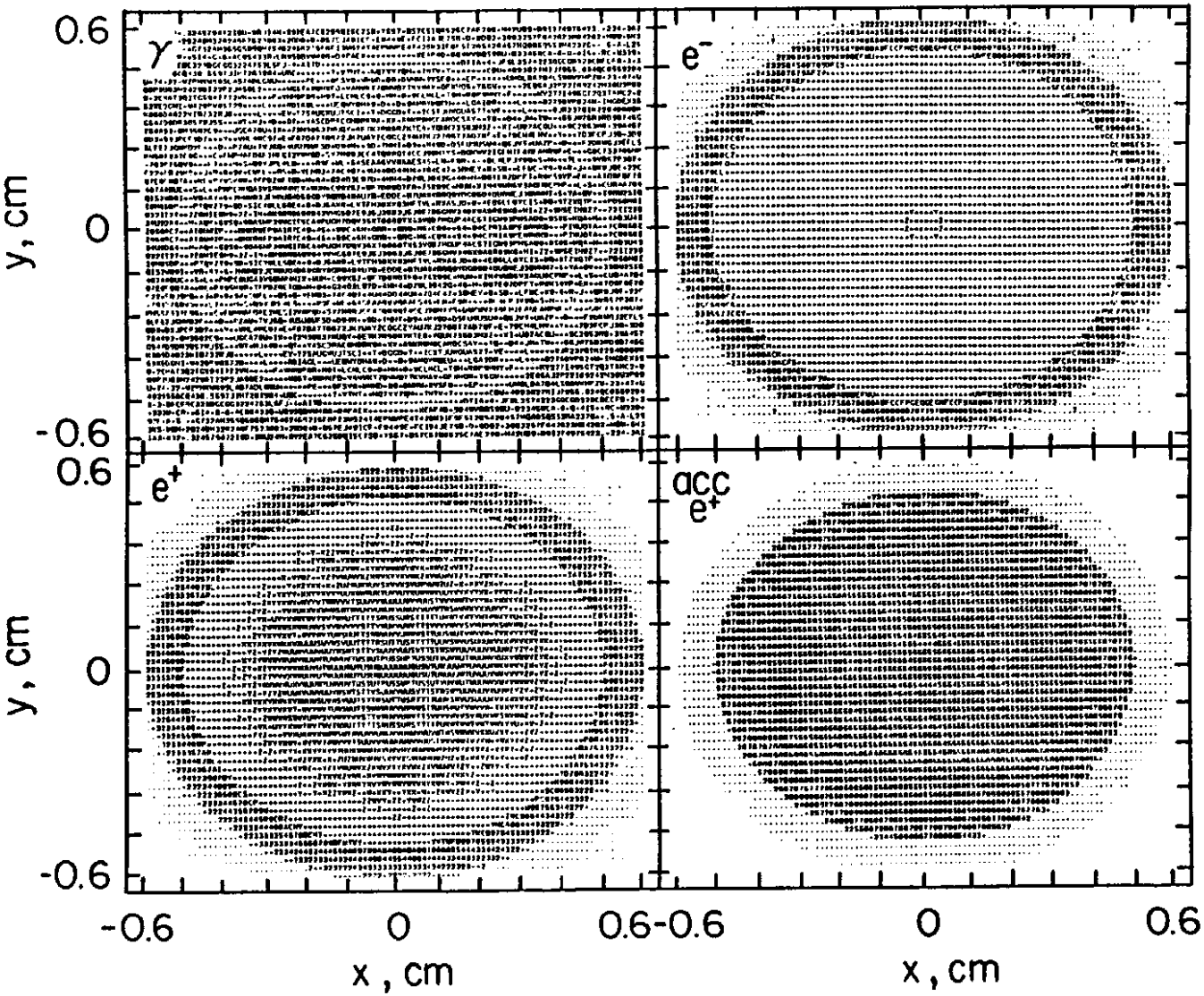

Fig. 8 Plots of x, y distribution for γs, e^-, e^+, and accepted e^+ at end of 100 cm long aluminum pipe target for incident angle of γ uniformly distributed between zero and 0.1 mrad.

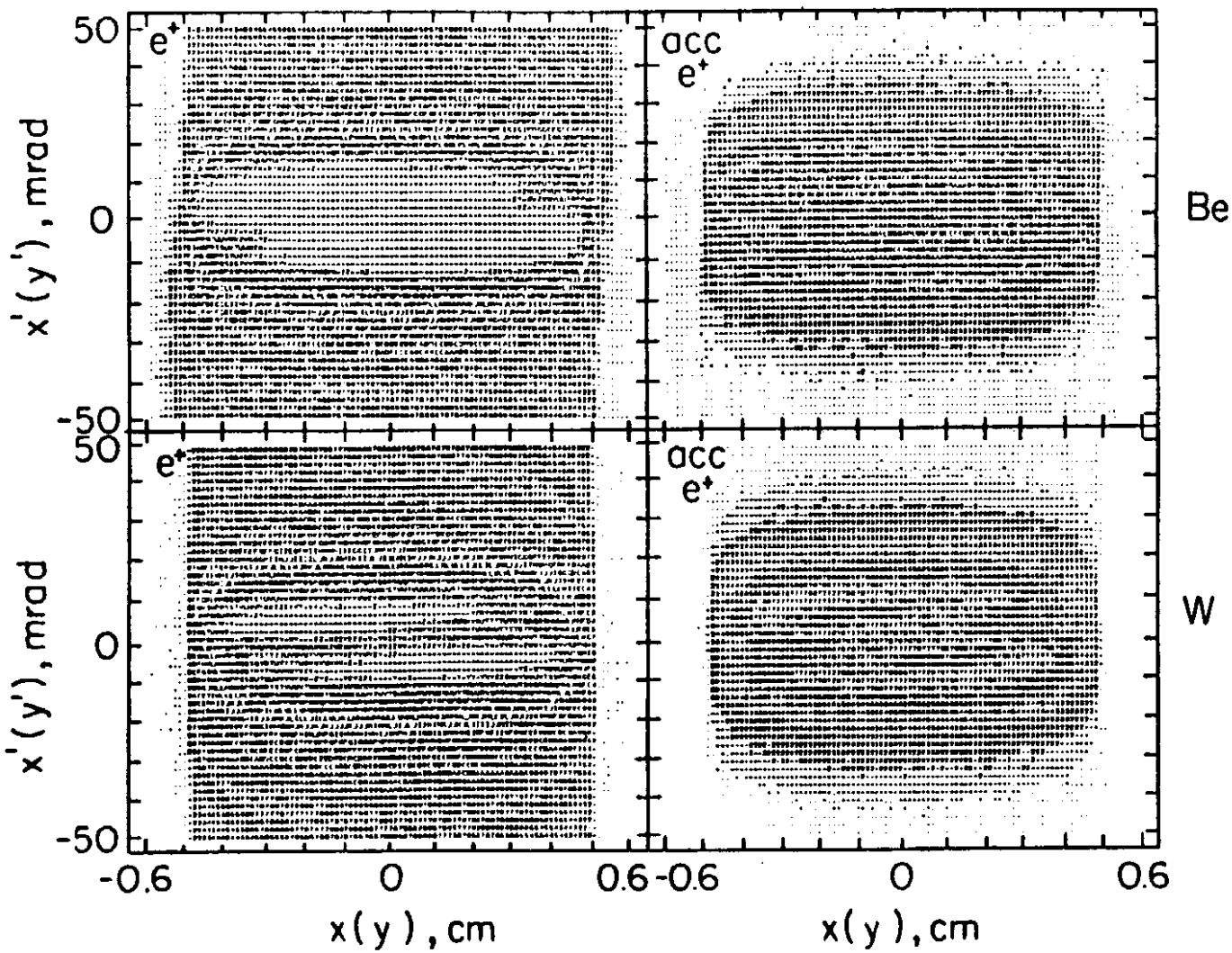

Fig. 9 Combined x, x' and y, y' plots for all e^+ and accepted e^+ at the end of a 100 cm long beryllium (top) and tungsten (bottom) pipe target for incident angle of γ uniformly distributed between zero and 0.1 mrad.

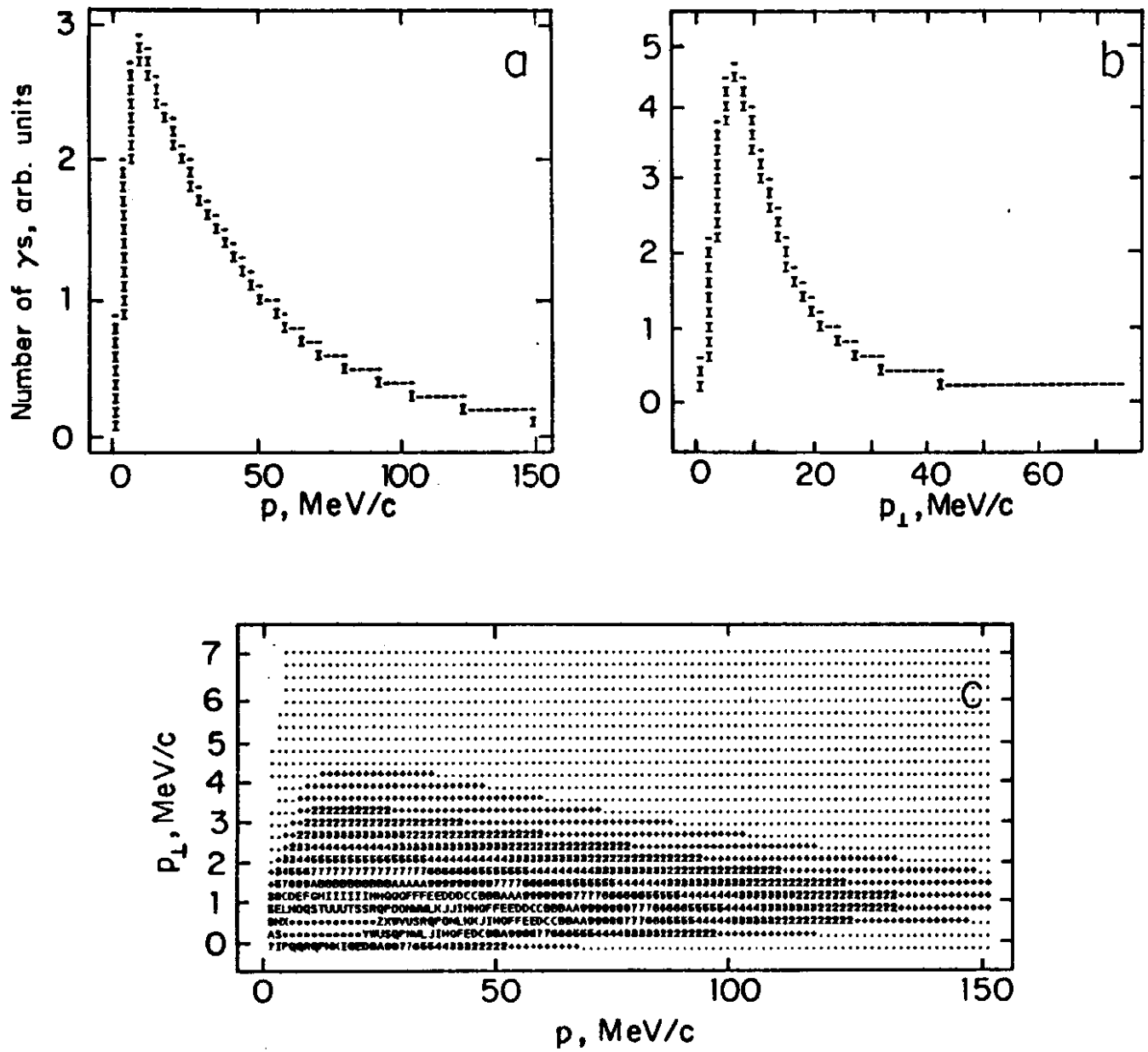

Fig. 10 (a) Momentum spectrum, (b) $p_\perp$ spectrum, and (c) joint distribution for all e^+ at end of 100 cm long aluminum pipe target for incident angle of γ uniformly distributed between zero and 0.1 mrad.

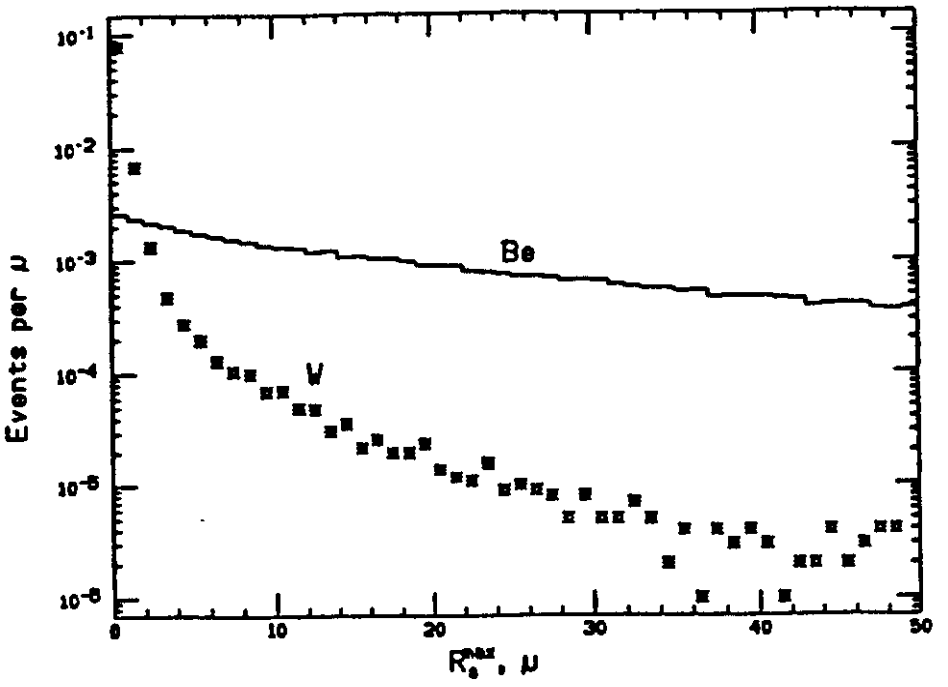

Fig. 11 Distribution of maximum radial excursion of electromagnetic showers leading to accepted e^+ for 100 cm long pipe of beryllium (histogram) and tungsten (stars) and for incident angle of γ uniformly distributed between zero and 0.1 mrad.

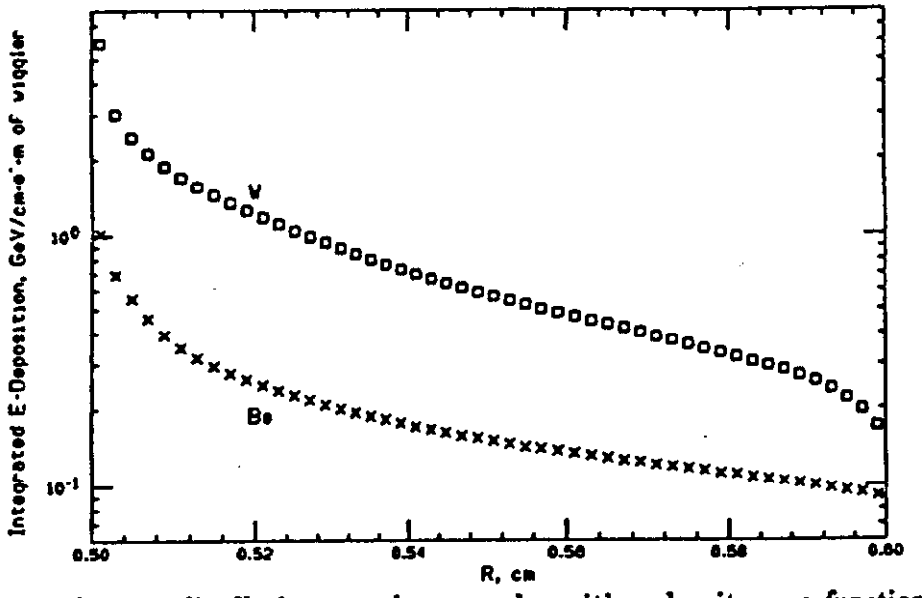

Fig. 12 Longitudinally integrated energy deposition density as a function of radius for 100 cm long pipe of beryllium (×) and tungsten (□) and for incident angle of γ uniformly distributed between zero and 0.1 mrad.

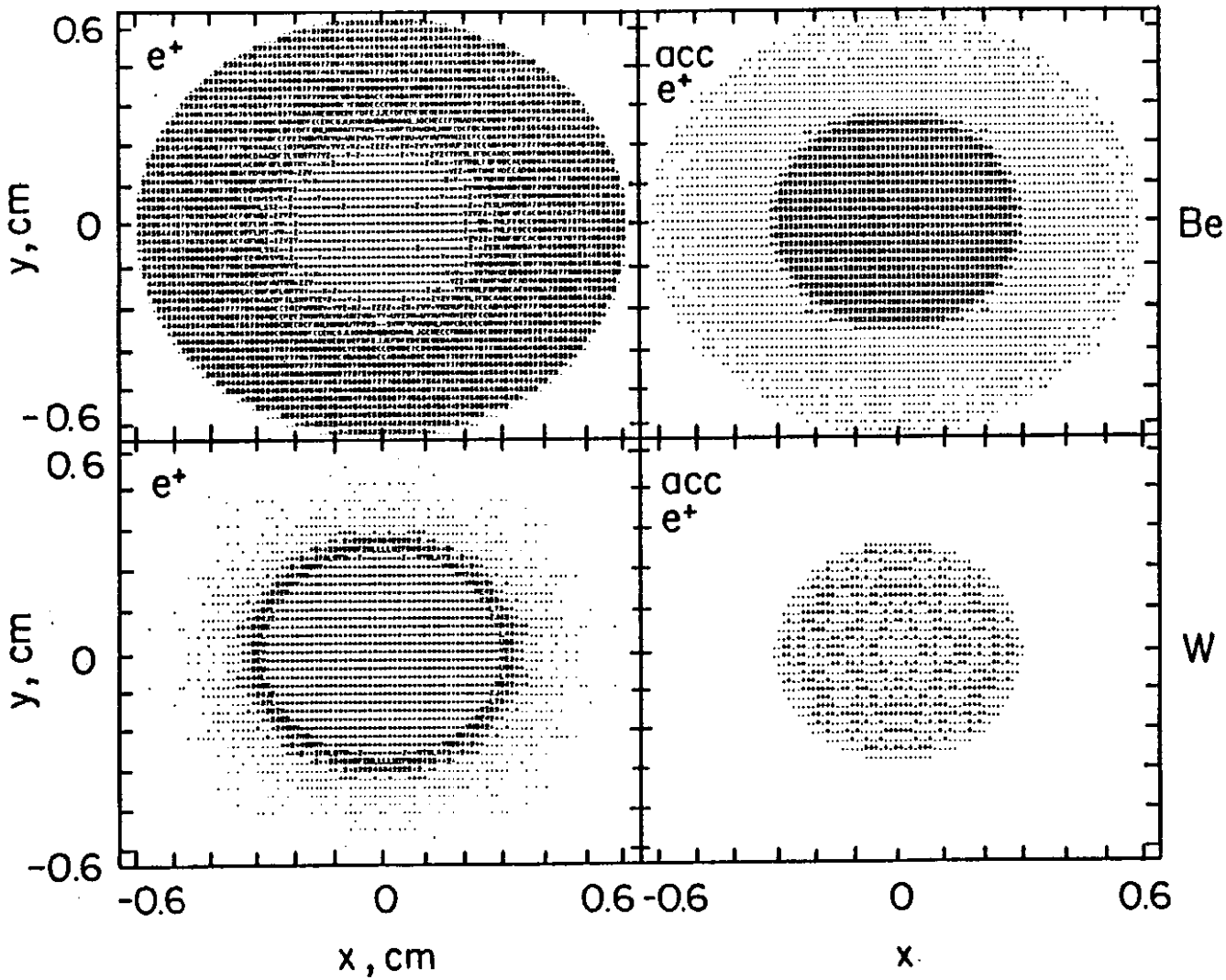

Fig. 13 Plots of x, y distribution for e^+ and accepted e^+ at end of solid target 0.4 radiation lengths long of beryllium (top) and tungsten (bottom). Beam is uniformly distributed over circle of 0.3 cm radius.

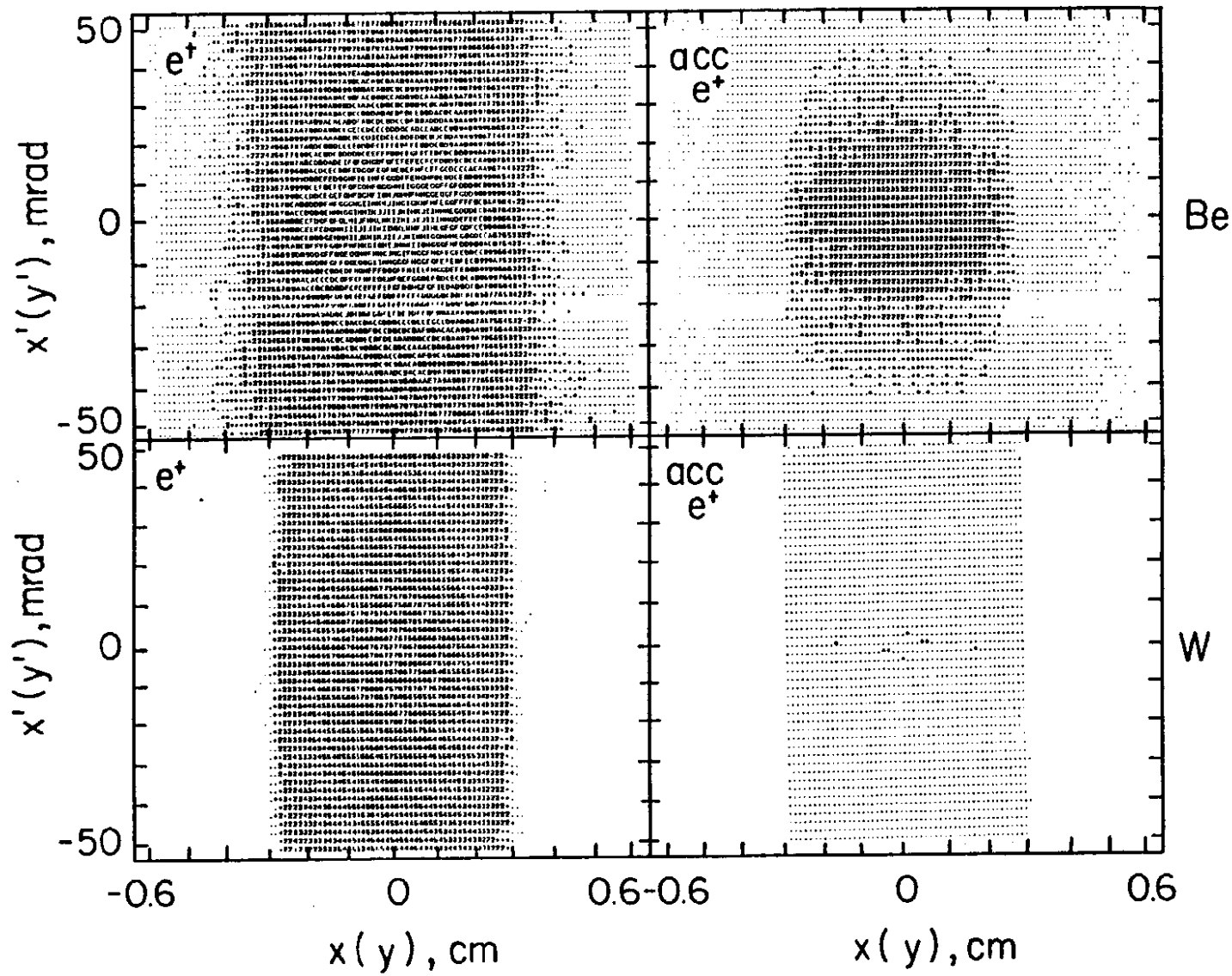

Fig. 14 Combined x, x' and y, y' plots for e^+ and accepted e^+ at end of solid target 0.4 radiation lengths long of beryllium (top) and tungsten (bottom). Beam is uniformly distributed over circle of 0.3 cm radius.

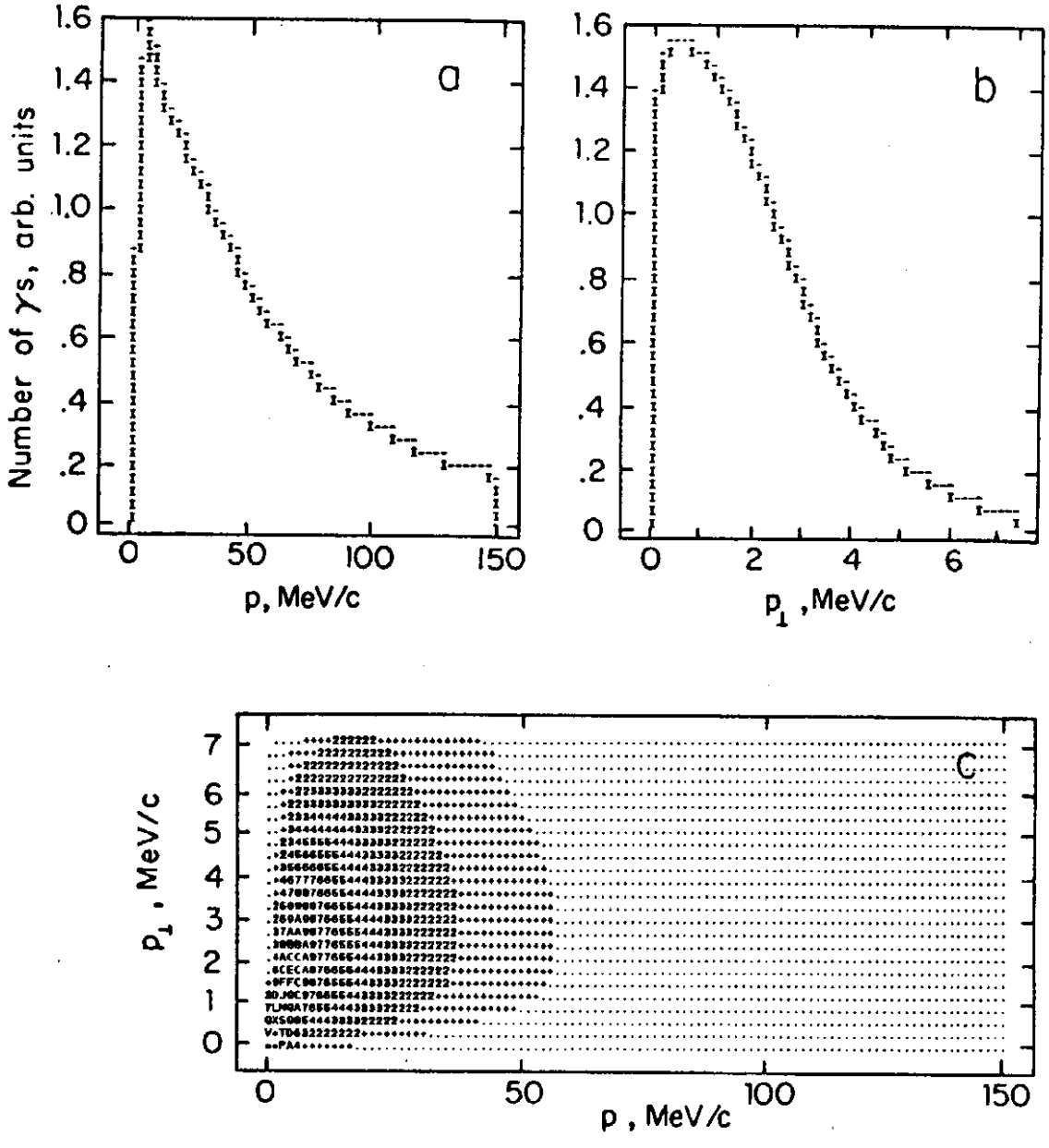

Fig. 15 (a) Momentum spectrum, (b) $p_\perp$ spectrum, and (c) joint distribution for all e^+ at end of 0.4 radiation lengths long solid aluminum target. Beam is uniformly distributed over circle of 0.3 cm radius.